



CHORUS

This is the accepted manuscript made available via CHORUS. The article has been published as:

Valley splitting in the van der Waals heterostructure $\text{WSe}_2/\text{CrI}_3$: The role of atom superposition

Zhiya Zhang, Xiaojuan Ni, Huaqing Huang, Lin Hu, and Feng Liu

Phys. Rev. B **99**, 115441 — Published 29 March 2019

DOI: [10.1103/PhysRevB.99.115441](https://doi.org/10.1103/PhysRevB.99.115441)

Valley splitting in a van der Waals heterostructure $\text{WSe}_2/\text{CrI}_3$: the role of atom superposition

Zhiya Zhang^{1,2}, Xiaojuan Ni², Huaqing Huang², Lin Hu², Feng Liu^{2,*}

¹*National & Local Joint Engineering Laboratory for Optical Conversion
Materials and Technology, Lanzhou University, Lanzhou 730000, China.*

²*Department of Materials Science and Engineering,
The University of Utah, Salt Lake City 84112, USA.*

*Corresponding author, Email: fliu@eng.utah.edu

(Dated: March 12, 2019)

Recent experiment shows that the $K'K$ valley degeneracy can be lifted in a monolayer WSe_2 deposited on a layered ferromagnetic substrate of CrI_3 . In this work, we take a van der Waals heterostructure $\text{WSe}_2/\text{CrI}_3$ to model the monolayer WSe_2 on the CrI_3 substrate and investigate the effects underpinning the $K'K$ valley splitting based on first-principles calculations. We demonstrate that the interfacial atom superposition plays an important role and a W-Cr superposition is essential for a relatively large valley splitting. The results indicate inevitable sample-to-sample variations in the $K'K$ valley splitting in the $\text{WSe}_2/\text{CrI}_3$. Furthermore, we show that the $K'K$ valley splitting can be tuned in a trilayer $\text{CrI}_3/\text{WSe}_2/\text{CrI}_3$ from nearly zero to more than two times of that in the bilayer $\text{WSe}_2/\text{CrI}_3$ by manipulating the layer alignment.

Keywords: valleytronics, valley degeneracy, valley splitting, WSe_2 , CrI_3 , atom superposition

I. INTRODUCTION

Valleytronics is rapidly emerging as an exciting field for both fundamental and applied research. It aims to control the valley rather than the electron spin and charge degrees of freedom to store information and perform logic operations. Atomically thin layered semiconductors, such as transition metal dichalcogenides (TMDs), have been considered as a wonderland for the research of valleytronics¹⁻⁷. In monolayer TMDs, inversion symmetry breaking together with strong spin-orbit coupling (SOC) lead to coupled spin and valley degrees of freedom. Time reversal symmetry requires the spin in the K' and K valleys to be opposite while energetically degenerate, resulting in a valley-spin locking relationship. Charge carriers in the two opposite valleys can be selectively excited by the right-hand (σ^+) and left-hand (σ^-) circularly polarized photons. However, due to the valley degeneracy, σ^+ and σ^- photoluminescence (PL) spectra always yield equal intensity and energy. Therefore, lifting the valley degeneracy has become an important research topic in the field of valleytronics. It is crucial to achieve large valley polarization, in analogous to large spin polarization in spintronics, for the development of valleytronics devices. A plenty of exotic properties such as quantum spin/valley anomalous Hall effect⁸⁻¹⁰, valley-dependent optoelectronics¹¹, spin/valley polarization of plasmons¹²⁻¹⁴, magneto-optical conductivity¹⁵, electrical transport of valley carriers¹⁶ have been explored in the valley-polarized systems. Moreover, valley polarization may interplay with spin polarization, especially to enhance spin polarization^{17,18}. Research efforts have been devoted to experimentally measuring valley currents, although disentangling valley currents from the currents carried by edge eigenstates remains challenging^{19,20}.

Previous research has shown multiple pathways to lift-

ing the $K'K$ valley degeneracy. One is to use ultrafast circularly polarized laser pump to break the valley degeneracy through the optical Stark effect^{3,4,21-23}. This approach allows for dynamic control of valley polarization but is limited by a quite short carrier lifetime (~ 1 ns). Another way is to apply a vertical magnetic field by taking advantage of the Zeeman effect^{6,24-26}. However, this effect turns out to be rather modest. For instance, in monolayer WSe_2 and MoSe_2 , the valley splittings were evaluated to be about 0.2 meV/T ^{6,25} and 0.12 meV/T ²⁴, respectively. Recent studies show that utilizing transition metal adsorption²⁷ or ferromagnetic semiconductor substrates such as EuO ⁷, EuS ²⁸ and CrI_3 ^{4,5} can achieve considerable valley splitting. In particular, layered substrate such as CrI_3 is favored for creating a relatively clean interface to eliminate the impurity scattering. Additionally, perpendicular van der Waals (vdW) heterostructure constructed from layered materials can minimize the effect of lattice mismatch that would weaken the valley splitting⁷. A hybrid system $\text{WSe}_2/\text{CrI}_3$ has recently been fabricated by transferring mechanically exfoliated monolayer WSe_2 onto CrI_3 substrate to lift the valley degeneracy^{4,5}. It was observed that σ^+ and σ^- spectra exhibit distinguishable energy and intensity. The $K'K$ valley splitting was accordingly extracted to be $\sim 3.5 \text{ meV}$, which was estimated to be equivalent to the effect of a magnetic field of 13 T ⁵.

In the present work, we aim to investigate the mechanisms underlying the $K'K$ valley splitting in the vdW heterostructure $\text{WSe}_2/\text{CrI}_3$ based on first-principles calculations. We show that the $K'K$ valley splitting is dependent of the stacking configurations where the interfacial atom superposition between the WSe_2 and CrI_3 varies. We discuss such effects on both the valence and conduction band valley splittings, which in turn make up the total $K'K$ valley splitting. Furthermore, we study

the valley splitting in a sandwich trilayer heterostructure $\text{CrI}_3/\text{WSe}_2/\text{CrI}_3$ to demonstrate further the critical role of the interfacial atom superposition in the valley degeneracy lifting. The rest of this paper is arranged as follows. In Sec. II we describe the method used. Results and discussion are presented in Sec. III. We conclude our work in Sec. IV.

II. METHODS

Our first-principles calculations are performed with the Vienna ab initio simulation package (VASP)^{29,30} based on density functional theory (DFT). The exchange-correlation potential is adopted in the form of Perdew-Burke-Ernzerhof (PBE)³¹ within the projector augmented wave (PAW) method³². The vdW heterostructures of bilayer $\text{WSe}_2/\text{CrI}_3$ and trilayer $\text{CrI}_3/\text{WSe}_2/\text{CrI}_3$ are constructed by stacking WSe_2 and CrI_3 layers on top of each other. The interlayer vdW interaction is described using the DFT-D3 method³³. A vacuum spacing of ~ 15 Å is used in order to avoid the interaction between the heterostructure and its periodic image. The reciprocal space is sampled by a Γ -centered k -mesh of $5 \times 5 \times 1$ in the first Brillouin zone for the structural optimization and $13 \times 13 \times 1$ for the static self-consistent calculation. An energy cutoff of 650 eV is used. Structural optimization is conducted by fully relaxing both the lattice constants and the atom positions until the convergence reaching less than 0.01 eV/Å for residual force on each atom and 1×10^{-7} eV for total energy. The SOC effect is included by performing a non-collinear calculation. The spin quantization axis is aligned vertical to the plane. The local magnetic moments on individual atoms can be rotated in- or out-of-plane. The GGA + U calculations^{34,35} have also been performed. It is noted that the calculated valley splitting is kept up to the submeV for relative comparison but may depend sensitively on the calculation details.

III. RESULTS AND DISCUSSION

A. Geometric structure of $\text{WSe}_2/\text{CrI}_3$

A bilayer vdW heterostructure of $\text{WSe}_2/\text{CrI}_3$ is constructed to model a monolayer WSe_2 deposited on a CrI_3 substrate. A 2×2 supercell of WSe_2 is used to match one unit cell of CrI_3 based on their respective lattice constants of 3.32 Å and 6.90 Å. A monolayer CrI_3 is used based on the fact that the ferromagnetism in bulk CrI_3 is well reproduced in the monolayer^{36,37}. Moreover, the effect of additional CrI_3 layer(s) on the valley splitting is found to be negligible from our test calculations.

Three typical stackings of C-1, C-2 and C-3 are considered for comparison, as shown in Fig. 1(a). Their specific features are: one Cr atom is directly above one Se atom in the C-1; one Cr is directly above one W in the C-2;

two Cr are directly above one Se and one W, respectively, in the C-3. Accordingly, the C-1 has a Se-Cr and the C-2 has a W-Cr atom superposition, respectively, while the C-3 accommodates the both. We use θ to represent the angle between a W-Cr connection to the vertical direction. In both the C-2 and C-3, $\theta = 0$ corresponding to a W-Cr superposition. As listed in Tab. I, the lattice constant (a) is the same and the interlayer spacing (d_{L_0}) is only slightly different between the three stackings. The optimized lattice constant of the $\text{WSe}_2/\text{CrI}_3$ is found to be closer to that of the WSe_2 which holds a relatively larger two dimensional elastic modulus (C_{2D}) (~ 286.9 and 109.7 Jm² for monolayer WSe_2 and CrI_3 , respectively). However, due to lattice mismatch, the two composites would not actually form a completely commensurate heterostructure, which has not been considered in our study. A more commensurate heterostructure could be made by making optimal choices between $\text{Cr}(\text{Br},\text{I})_3$ and $(\text{Mo},\text{W})(\text{S},\text{Se},\text{Te})_2$. The underlying physics should be similar to that of the $\text{WSe}_2/\text{CrI}_3$ we studied here.

The interlayer binding energy E_b is defined as $E_b = (E_{\text{heter}} - E_{\text{WSe}_2} - E_{\text{CrI}_3})/N$ with E_{heter} , E_{WSe_2} and E_{CrI_3} being the total energies of the optimized heterostructure, the monolayer WSe_2 and CrI_3 , respectively, and N ($N = 20$) is the total number of atoms in the heterostructure. Only a small energy barrier exists between different structures due to a similar E_b , so that all the structures might be obtained experimentally. To reveal the W-Cr coupling, the distribution of the W-Cr distance ($d_{\text{W-Cr}}$) in the three stackings is shown in Fig. 1(b). In addition, the first nearest-neighbor (NN) W-Cr distance $d_{1\text{NN}}$ and the average W-Cr distance \bar{d} are given in Fig. 1(c).

B. K' valley splitting in $\text{WSe}_2/\text{CrI}_3$

The calculated band structures are similar for the three stackings, as represented by that of the C-3 in Fig. 2(c). The K' and K valleys of WSe_2 is well preserved in the heterostructures. We note that the K and K' of the primitive cell is folded to the K' and K of the 2×2 supercell of WSe_2 , respectively. The band gap remains direct at the K' (K) point similar to the case of free-standing monolayer WSe_2 despite a tiny tensile strain ($\sim 0.2\%$, as listed in Tab. I) was introduced to WSe_2 in the heterostructures. Tensile strain can induce a direct-indirect band gap transition in monolayer TMDs³⁸⁻⁴¹, which has not been observed in the $\text{WSe}_2/\text{CrI}_3$ due to the very small tensile strain ($\sim 0.2\%$) introduced in the WSe_2 . Both the valence band (VB) and conduction band (CB) of WSe_2 are dominated by W atoms, with the VB by $W-d_{x^2-y^2/xy}$ and the CB by $W-d_{z^2}$ orbitals, respectively. The atomic orbitals of Se- $p_{x/y/z}$ and W- $s/p_{x/y}/d_{yz}$ are slightly involved, as listed in Tab. S1 of the Supplemental Material⁴⁴.

The valley-spin subbands are labeled as $\text{VB1}'$, $\text{CB1}'$, VB2 and CB2 for the spin-up states and $\text{VB2}'$, $\text{CB2}'$,

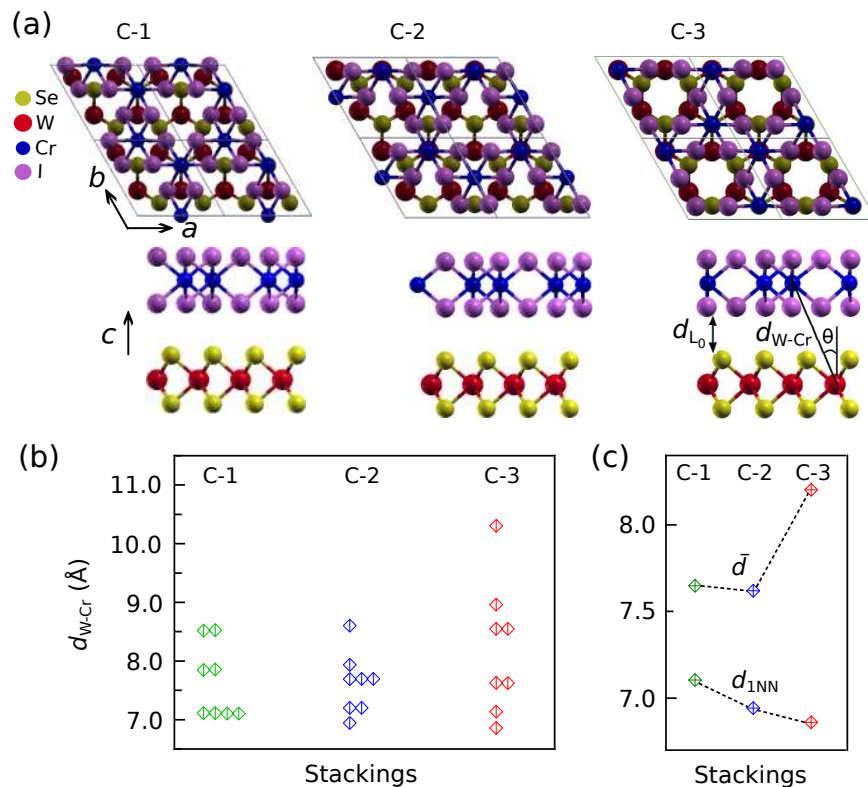


FIG. 1. (a) Top (top panels) and side (bottom panels) views of WSe₂/CrI₃ in three stackings of C-1, C-2 and C-3. The d_{L_0} and d_{W-Cr} denote the interlayer spacing and W-Cr distance, respectively. The θ refers to the angle of a W-Cr connection to the vertical direction. (b), (c) The W-Cr distance distribution in the supercell of the three stackings. The d_{1NN} and \bar{d} represent the first nearest-neighbor and the average W-Cr distance, respectively.

TABLE I. Comparison between three stackings of WSe₂/CrI₃. The a denotes the optimized lattice constant and d_{L_0} the equilibrium interlayer spacing. The third column is the strain introduced in the WSe₂. The E_b represents the interlayer binding energy per atom. The Δ_{VB} , Δ_{CB} and $\Delta_{K'K}$ stand for the valence band, conduction band and total valley splittings, respectively.

Stacking	a (Å)	Strain	d_{L_0} (Å)	E_b (meV)	Δ_{VB} (meV)	Δ_{CB} (meV)	$\Delta_{K'K}$ (meV)
C-1	6.65	0.2%	3.58	-52.4	-0.05	0.26	0.31
C-2	6.65	0.2%	3.68	-49.2	-0.81	-0.12	0.69
C-3	6.65	0.2%	3.59	-51.8	-1.13	-0.09	1.04

VB1 and CB1 for the spin-down ones, respectively, as shown in Fig. 2(b) and (c). The K' and K valleys are energetically degenerate in pristine monolayer WSe₂, as illustrated by the energy diagram in Fig. 2(a). When WSe₂ is put on a ferromagnetic substrate of CrI₃, the $K'K$ valley degeneracy is lifted, as depicted by the energy diagram in Fig. 2(b). According to our calculations, there is nearly zero magnetic moment induced on the W and Se atoms by the CrI₃ substrate and the exchange interaction is therefore negligible. The mechanisms underlying the valley splitting in the WSe₂ placed on the CrI₃ should be different from that observed in WSe₂/EuO⁷, WSe₂/EuS²⁸ and graphene deposited on the ferromagnetic films of EuO, EuS, CoFe₂O₄ and Y₃Fe₅O₁₂^{42,43}. In the latter ones, charge transfer occurs between the composites and a finite magnetic moment is induced in

the WSe₂ and graphene by the substrates. The case of the WSe₂/CrI₃ is more similar to the situation when WSe₂ is exposed to an external magnetic field. In addition, the electrostatic potential gradient between WSe₂ and CrI₃ should also play a role in lifting the valley degeneracy. Previous studies demonstrated that applying a vertical external electric field combining with a magnetic field can significantly increase the valley splitting in silicene^{8-10,12,14}. Similar effects might be at function here in the WSe₂/CrI₃, where a vertical electric field is generated from an interlayer electrostatic potential gradient as shown in Fig. 2(d). However, such an interlayer electric field appears weak, as detailed in S1 of the Supplemental Material⁴⁴.

We will focus on the subbands VB1', CB1', VB1 and CB1 in the following discussion for the sake of simplicity.

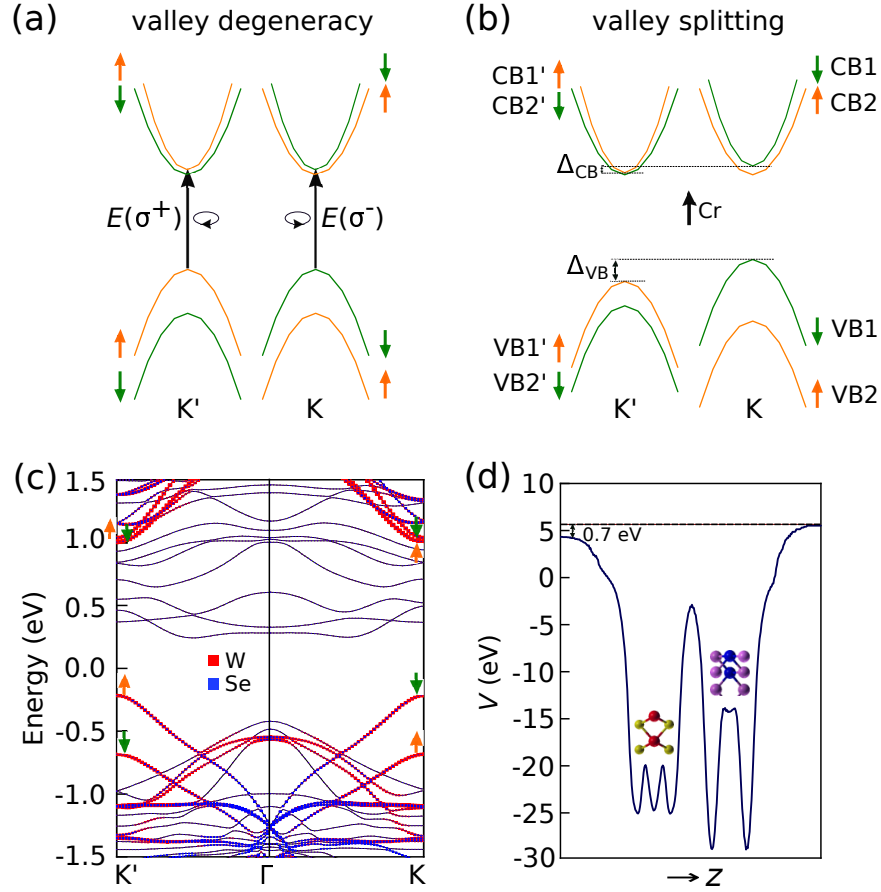


FIG. 2. (a) Energy diagram indicating the $K'K$ valley degeneracy. $E(\sigma^+)$ and $E(\sigma^-)$ represent the interband optical transition energies of right-hand (σ^+) and left-hand (σ^-) circularly polarized photons, respectively. The spin-up and spin-down valley-spin states are denoted with orange up- and green down-arrows, respectively. (b) Energy diagram depicting the $K'K$ valley degeneracy lifting. The Δ_{VB} and Δ_{CB} stand for the valence and conduction band valley splittings, respectively. The magnetization axis of the CrI_3 , *i.e.* the Cr spin is aligned vertical upward as denoted by the black up-arrow. (c) Atom-projected band structure of $\text{WSe}_2/\text{CrI}_3$ in the C-3 stacking. (d) Electrostatic potential (V) in the C-1, C-2 and C-3.

These subbands are involved in the optical excitation and the valley polarization of WSe_2 and WS_2 ^{4,5,16,28}. In contrast, the effects of the subbands $\text{VB2}'$, $\text{CB2}'$, VB2 and CB2 are largely suppressed due to a rather large valence band SOC splitting (> 450 meV). The total $K'K$ valley splitting can be derived as $\Delta_{K'K} = (E_{\text{CB1}'} - E_{\text{VB1}'}) - (E_{\text{CB1}} - E_{\text{VB1}})$ or $\Delta_{K'K} = \Delta_{\text{CB}} - \Delta_{\text{VB}}$, which includes the VB and CB valley splittings of $\Delta_{\text{VB}} = E_{\text{VB1}'} - E_{\text{VB1}}$ and $\Delta_{\text{CB}} = E(\text{CB1}') - E(\text{CB1})$, respectively. Due to the conservation of angular momentum required by optical transition selection rules and the opposite valley angular momentum in the K' and K valleys, electrons in the two valleys can be selectively excited by the σ^+ and σ^- photons, respectively. Accordingly, the $K'K$ valley splitting can be characterized by the optical transition energy difference between the $E(\sigma^+)$ and $E(\sigma^-)$, *i.e.* $\Delta_{K'K} = E(\sigma^+) - E(\sigma^-)$. In addition, we list the valley splitting between the $\text{VB2}'$ and VB2 and that between the $\text{CB2}'$ and CB2 in Tab. S2 of the Supplemental Material⁴⁴ for reference. It is worth noting that the GGA

+ U ($J = 0.7$ eV and $U = 2.7$ eV)³⁵ and the standard GGA calculations produce nearly the same magnetic moment ($\approx 3 \mu\text{B}$) per Cr atom and almost identical valley splitting.

C. Stacking-dependent $K'K$ valley splitting in $\text{WSe}_2/\text{CrI}_3$

The valley splitting in the $\text{WSe}_2/\text{CrI}_3$ is found to be stacking-dependent. As shown in Tab. I, among the three stackings, the C-1 has the smallest (0.31 meV) while the C-3 has the largest $\Delta_{K'K}$ (1.04 meV). This trend has been maintained when the interlayer spacing between the WSe_2 and CrI_3 is arbitrarily reduced (Fig. 3(a)). Since the electronic states in the K' and K valleys are mainly contributed from the W atoms as mentioned above, and meanwhile the Cr atoms are the main species providing the local magnetic field, the W-Cr coupling is expected to play a crucial role in splitting the $K'K$ valley. Our

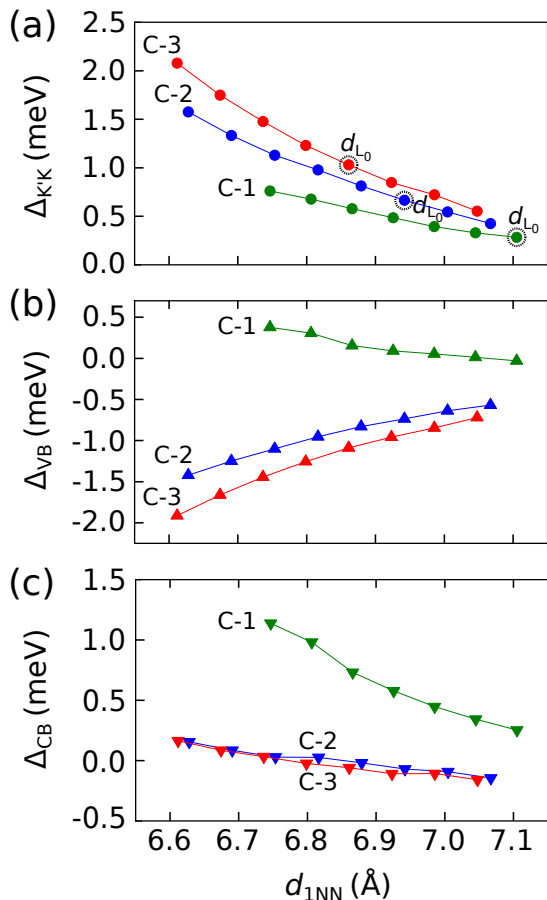


FIG. 3. Dependence of (a) total ($\Delta_{K'K}$), (b) valence band (Δ_{VB}) and (c) conduction band (Δ_{CB}) valley splittings on the first nearest-neighbor W-Cr distance d_{1NN} in the C-1, C-2 and C-3. The results are obtained by reducing or expanding the interlayer separation (d_L) in reference to the equilibrium interlayer spacing (d_{L_0}).

calculations demonstrate two major influencing factors:

(i) The first NN W-Cr distance (d_{1NN}). Generally, a short W-Cr distance results in a strong W-Cr coupling and a relatively large valley splitting. It is found that the d_{1NN} ($d_{1NN(C-1)} > d_{1NN(C-2)} > d_{1NN(C-3)}$) reflects well the trend of the $\Delta_{K'K}$ ($\Delta_{K'K(C-1)} < \Delta_{K'K(C-2)} < \Delta_{K'K(C-3)}$), as shown in Fig. 3(a). As a counter example, the average W-Cr distance (\bar{d}) is much smaller in the C-1 than in the C-3 (figure 1(c)), which is obviously inconsistent with the trend of $\Delta_{K'K}$ going from C-1 to C-3.

(ii) The angle of the first NN W-Cr to the vertical direction (θ_{1NN}). As can be found in Fig. 3(a), even with the same d_{1NN} , $\Delta_{K'K}$ is still smaller in the C-1 than in the C-2 and C-3. The different angles of the first NN W-Cr to the vertical direction, namely θ_{1NN} , can be possibly accounted for such difference. In the C-2 and C-3, $\theta_{1NN} = 0$ which corresponds to a perfect W-Cr superposition. In contrast, in the C-1, $\theta_{1NN} = 15.55^\circ$, a less perfect W-Cr superposition.

The above two aspects are also reflected when one translates the CrI_3 layer along the a axis relatively to the WSe_2 layer. The results are similar for the layer translating along the b axis (not shown). The layer translation results in decreased $\Delta_{K'K}$ in both the C-2 and C-3 (top panels, Figs. 4(b) and (c)), because it reduces the W-Cr superposition. When only one Cr is near one W (from top views), as seen in insets C-25 and C-34 of Figs. 4(b) and (c), respectively, $\Delta_{K'K}$ becomes the smallest. Thereafter, the structure starts to recover gradually to the starting configuration, and $\Delta_{K'K}$ increases correspondingly. In a striking contrast, the trend is opposite in the C-1 (top panel, Fig. 4(a)). This is because the layer translation makes the W move closer to the Cr (inset C-14 of Fig. 4(c)). Total energy changes with the layer translation can be found in Fig. S1 of the Supplemental Material⁴⁴.

In all the three stackings, the changes in $\Delta_{K'K}$ correspond well with the changes in d_{1NN} (Figs. 4(d)-(f)). It is further verified by a full layer translating (for the C-3 stacking as a representative case), as shown in Fig. 5. This is also the case for the θ_{1NN} (not shown). In fact, the d_{1NN} is correlated with the θ_{1NN} through $d_{1NN} = D / \cos \theta_{1NN}$ with D being about 6.85, 6.94 and 6.86 Å in the C-1, C-2 and C-3, respectively. Additionally, it is interesting to find that the $\Delta_{K'K}$ of the stacking represented by inset C-36, where there are two W and each has a nearby Cr, is smaller than that of the C-3 which has one W superimposed on one Cr. This result is a powerful illustration of the critical role of the W-Cr superposition in producing a relatively large $\Delta_{K'K}$. It suggests a sample-to-sample variation of the valley splitting in the $\text{WSe}_2/\text{CrI}_3$, and a site-specific transfer technique¹⁶ would be helpful to optimize the device performance in actual applications. Besides, according to previous studies in the graphene system^{42,43,45}, the atomic environmental difference between the W atoms relative to the CrI_3 substrate should be beneficial to promoting the valley splitting in the WSe_2 (see S2 and Fig. S2 of the Supplemental Material⁴⁴).

It is noted that our calculated valley splitting (~ 1 meV) is relatively smaller than that experimentally observed (~ 3 meV)⁵. The difference is considered to be reasonable in view of that the calculated valley splitting is dependent of the computational details. Moreover, the valley splitting appears small and low temperature condition may be necessary in the applications. Exploring large valley splitting in the TMDs-based heterostructures requires further research in the future.

D. The valence (Δ_{VB}) and conduction band valley splitting (Δ_{CB})

In the $\text{WSe}_2/\text{CrI}_3$, the Δ_{VB} is much larger in magnitude than the Δ_{CB} and dominates the total valley splitting except for the peculiar case of the C-1 stacking. The coupling between the valley-spin states in the VB and the magnetic field of the substrate can be visually described

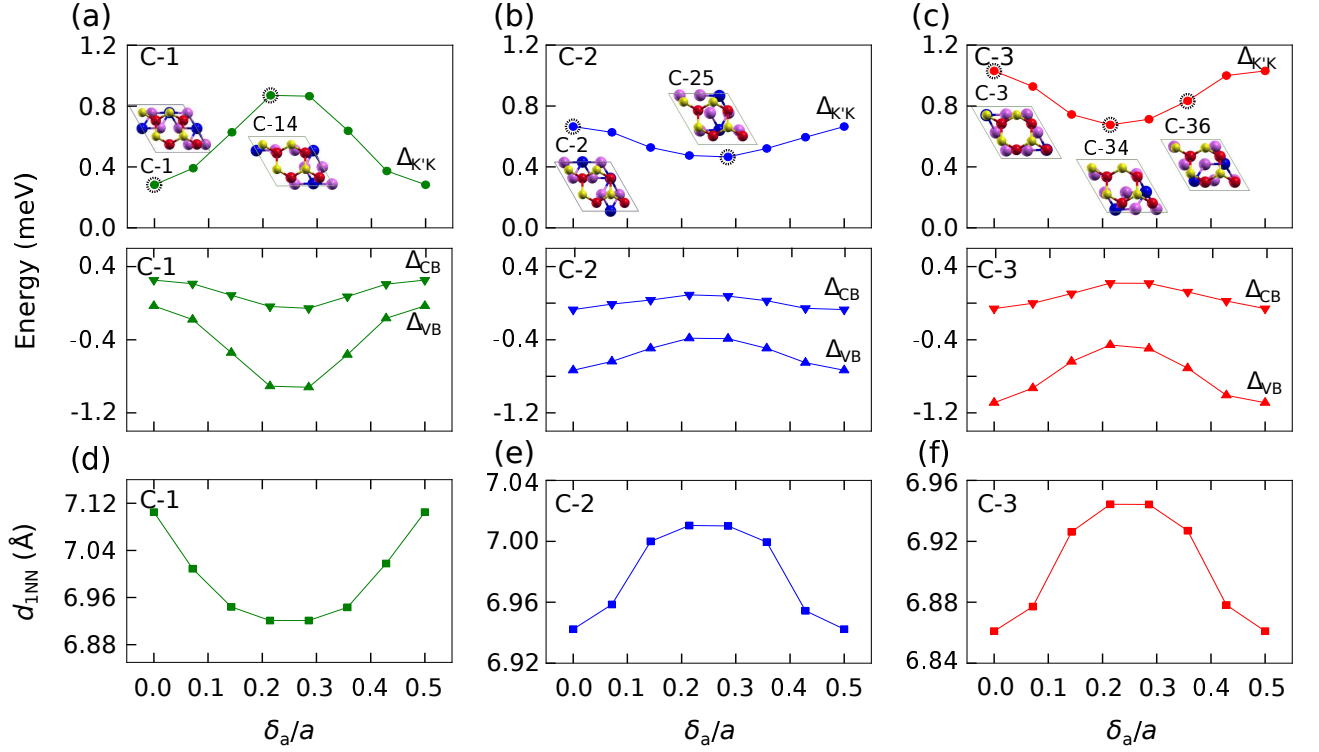


FIG. 4. Rigid translating the CrI_3 layer relative to the WSe_2 layer along the a direction in the C-1, C-2 and C-3. (a), (b), (c) Evolution of total valley splitting ($\Delta_{K'K}$, top panels), and valence and conduction band valley splittings (Δ_{VB} and Δ_{CB} , bottom panels). The insets represent typical stacking configurations during the layer translation. (d), (e), (f) The changes in the first nearest-neighbor W-Cr distance (d_{1NN}). δ_a/a represents the fractional layer shift. The structures at $\delta_a/a = 0.5$ are identical to the corresponding starting configurations.

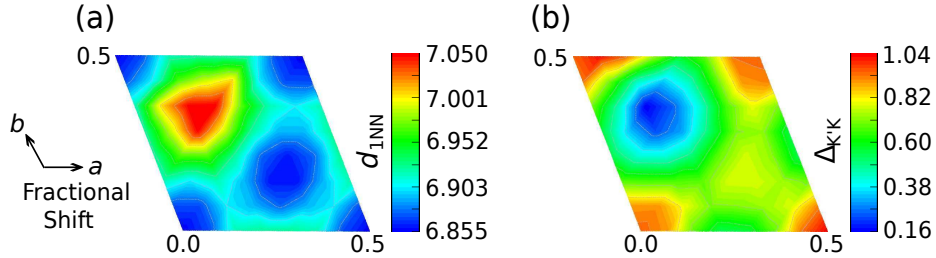


FIG. 5. Full rigid layer translation for the C-3 stacking. Evolution of the first nearest-neighbor W-Cr distance (d_{1NN}) (a) and total valley splitting ($\Delta_{K'K}$) (b).

by an alignment between the valley spin and the Cr spin. As illustrated in Fig. 2(b), the valley spin aligned in parallel with the Cr spin has relatively lower energy, *i.e.* $\Delta_{VB} < 0$. This feature is manifested in the C-2 and C-3 when the d_L is reduced (the C-2 and C-3 curves, Fig. 3(b)) and in all the three stackings when the CrI_3 layer is laterally shifted relative to the WSe_2 layer (the Δ_{VB} curves, Figs. 4(a)-(c)).

The weak CB valley splitting is related to the atomic composition nature. As mentioned above, the CB is dominated by the $\text{W-}d_{z^2}$ ($m_l = 0$). The zero m_l of the $\text{W-}d_{z^2}$ leads to a weak coupling of the valley-spin states with the magnetic field of the substrate and hence a smaller CB valley splitting. In addition, the Δ_{CB} should also be

interlinked with the Δ_{VB} considering spin splitting in the CB of the TMDs is associated with that in the VB^{46,47}. A combination of DFT calculations and multiband Hamiltonian model study has been performed to understand the chemical origin the CB spin splitting^{46,47}. In addition to the first-order contribution from the p orbital of the chalcogen atom (X), the second-order contribution from remote bands also appears important, especially for the WX_2 compared to the MoX_2 . In the present case, a correlated change in the Δ_{VB} and Δ_{CB} is seen in Figs. 4(a)-(c). However, the detailed understanding of the valley splitting in the CB requires further study.

The peculiarity of the C-1 stacking is that the Δ_{CB} is positive and it is larger than the Δ_{VB} in magnitude.

Since the former feature weakens and the latter one vanishes with translating the CrI_3 layer (bottom panels, Figs. 4(a)-(c)), it should be closely related to the structural characteristics of the C-1 stacking, that is, the Se-Cr superposition. We noticed that the $\text{Se-}p_z$ and $\text{Se-}p_{x/y}$ orbitals carry opposite spin in the conduction band $\text{CB1}'$ (CB1), so that they will shift the $\text{CB1}'$ (CB1) oppositely in energy. Surprisingly, the effect of the $\text{Se-}p_z$ overtakes that of the $\text{Se-}p_{x/y}$, resulting in $\Delta_{\text{CB}} > 0$. Such an effect is reinforced by reducing the d_L (the C-1 curve, Fig. 3(c)). In this situation, due to the interband interaction, Δ_{VB} also becomes positive (the C-1 curve, Fig. 3(b)). The $\text{Se-}p_z$ effect (*i.e.* $\Delta_{\text{CB}} > 0$) also emerges in the C-2 and C-3 with reducing the interlayer spacing (the C-2 and C-3 curves, Fig. 3(c)). Accordingly, it should be correlated with the interlayer coupling effect. We emphasize that the $\text{Se-}p_z$ effect appears observable only when the VB valley splitting (W-Cr coupling) is weak. Recently, researchers have begun to realize the complexity of the interlayer coupling arising from the p_z orbital in TMDs^{48–50}. Interestingly, in bilayer MoS_2 , a pressure induced increase of the interaction between the $\text{S-}p_z$ orbitals is observed to lead to a considerable spin splitting without considering the SOC effect⁴⁹.

In all the above discussion, both the spin quantization axis of the WSe_2 and the magnetization axis of the CrI_3 (*i.e.* the Cr spin) are aligned along the c axis. We label the case as $\uparrow\uparrow$. If we flip the magnetization axis of the CrI_3 upside down, as represented by $\uparrow\downarrow$, the energy shift of the valley-spin band will be reversed while the valley splitting magnitude remains almost unchanged (see Tab. S3 of the Supplemental Material⁴⁴). This phenomenon is similar to what observed in WSe_2 subjected to a vertical external magnetic field where a reversed magnetic field results in an opposite energy shift of the valley-spin band^{5,6,25,28}. If we artificially confine the Cr spin within the CrI_3 layer, the valley splitting nearly vanishes. It is worth mentioning that in the case of $\uparrow\uparrow$, $\Delta_{\text{K}'\text{K}}$ have positive signs (Fig. 3(a) and Figs. 4(a)-(c)). Correspondingly, the σ^+ PL spectrum will exhibit a higher energy than the σ^- one, which coincides with the previous experimental observation⁵. While in the case of $\uparrow\downarrow$, the σ^+ spectrum will present a relatively lower energy than the σ^- one. Due to the energy degeneracy between the $\uparrow\uparrow$ and $\uparrow\downarrow$ states, they both could be observed experimentally.

E. The $\text{K}'\text{K}$ valley splitting in $\text{CrI}_3/\text{WSe}_2/\text{CrI}_3$

The influence of thickness of the CrI_3 substrate on the valley splitting is negligible. We have increased the CrI_3 from monolayer to two and three layers with the Cr spins in two adjacent CrI_3 layers aligning in opposite direction^{36,37,51}. The resultant valley splitting is nearly unchanged. On the other hand, if we sandwich the WSe_2 between two CrI_3 sheets, the valley splitting can be changed significantly. Three typical stackings of

TABLE II. Comparison between three stackings of $\text{CrI}_3/\text{WSe}_2/\text{CrI}_3$. The a , d_L and $\Delta_{\text{K}'\text{K}}$ are defined with the same convention in Tab. I. The first and third arrows as bracketed represent the opposite Cr spins in the two CrI_3 sheets and the second arrow denotes the spin quantization of the WSe_2 .

Stacking	$a(\text{\AA})$	$d_L(\text{\AA})$	$\Delta_{\text{K}'\text{K}}(\text{meV})(\uparrow\downarrow)$	$\Delta_{\text{K}'\text{K}}(\text{meV})(\uparrow\uparrow)$
C-11	6.69	3.55	-0.01	1.39
C-33	6.69	3.57	-0.03	3.03
C-13	6.69	3.59	-0.86	1.25

$\text{CrI}_3/\text{WSe}_2/\text{CrI}_3$ are considered, as displayed in Fig. S3 of the Supplemental Material⁴⁴. The C-11 and C-33 are constructed based on the C-1 and C-3, respectively, and the C-13 is a hybrid of the C-1 and C-3. The structural parameter (Tab. II) is only slightly different and the band structure (see Fig. S4 of the Supplemental Material⁴⁴) is similar compared to that of the bilayer $\text{WSe}_2/\text{CrI}_3$. Two spin alignments of the CrI_3 layers are considered to study the valley splitting properties. In the first case, the Cr spins in the top and bottom CrI_3 sheets are aligned antiparallel. We label this case as $\uparrow\downarrow$, where the first and third arrows represent the opposite Cr spins in the two CrI_3 sheets and the second arrow denotes the spin quantization axis of the WSe_2 . It is interesting to find that the magnetic field effect from the two CrI_3 sheets nearly cancels, resulting in a nearly vanishing valley splitting in both the C-11 and C-33, as listed in Tab. II. The valley splitting is not exactly zero mainly due to the atom conjugations within the WSe_2 and CrI_3 layers.

In the second case, the Cr spin are aligned parallel between the two CrI_3 sheets, denoted as $\uparrow\uparrow$. The resultant $\Delta_{\text{K}'\text{K}}$ is more than two times of that in the bilayer $\text{WSe}_2/\text{CrI}_3$. Most interestingly, for the C-13 stacking in the case of $\uparrow\downarrow$, the magnetic field effects from the two CrI_3 sheets tend not to cancel and the $\Delta_{\text{K}'\text{K}}$ adopts a considerable value of 0.86 meV. These results verify again the critical role of the interfacial atom arrangement on the valley splitting in the $\text{WSe}_2/\text{CrI}_3$. Actually, the two states of $\uparrow\downarrow$ and $\uparrow\uparrow$ are energetically degenerate, but have very different valley splitting. One may pre-treat a trilayer $\text{CrI}_3/\text{WSe}_2/\text{CrI}_3$ sample in a magnetic field to make the Cr spins in the two CrI_3 sheets align parallel, in order to achieve an enhanced valley splitting. This prediction might be tested by future experiments. In real device, it might be hard to synthesize a trilayer structure exactly as the C-11 or C-33. In comparison, fabricating a trilayer by sandwiching monolayer WSe_2 between any two identical CrI_3 sheets is possibly more feasible. In any case, trilayer $\text{CrI}_3/\text{WSe}_2/\text{CrI}_3$ are ideal structures to verify the atom superposition effect observed in the bilayer $\text{WSe}_2/\text{CrI}_3$.

IV. CONCLUSION

We have demonstrated that the $K'K$ valley splitting in the heterostructure of WSe_2/CrI_3 depends critically on the interfacial atom superposition based on a comparative study of bilayer WSe_2/CrI_3 and trilayer $CrI_3/WSe_2/CrI_3$ of different stackings. The results suggest a sample-to-sample variation of the $K'K$ valley splitting in the WSe_2/CrI_3 . The valley splitting magnitude is primarily influenced by the first nearest-neighbor W-Cr distance and the angle of the first nearest-neighbor W-Cr to the vertical direction. The coupling between the valley spin in the valence band and the magnetic field of the CrI_3 substrate predominates the total valley splitting. The conduction band valley splitting is weak and varies with a combined effect of the interband interaction

and the $Se-p_z$ effect. These findings further our basic understanding of the ferromagnetic substrate effect on the valley degeneracy lifting in TMDs-based heterostructures beyond the WSe_2/CrI_3 and provide a useful guide to the valleytronic control in realistic applications.

ACKNOWLEDGMENTS

Z. Zhang acknowledges financial support from the Science Foundation of Gansu Province (17JR5RA200). X. Ni, H. Huang, and F. Liu acknowledge the support from U.S. DOE-BES (Grant No. DE-FG02-04ER46148). We also acknowledge DOE-NERSC and CHPC at the University of Utah and Fermi at Lanzhou University for providing the computing resources.

-
- ¹ D. Xiao, G. B. Liu, W. Feng, X. Xu, and W. Yao, *Phys. Rev. Lett.* **108**, 196802 (2012).
- ² T. Cao, J. Feng, J. Shi, Q. Niu, and E. Wang, *Nat. Commun.* **3**, 887 (2012).
- ³ K. F. Mak, K. He, J. Shan, and T. F. Heinz, *Nat. Nanotech.* **7**, 494–498 (2012).
- ⁴ K. L. Seyler, D. Zhong, B. Huang, X. Linpeng, N. P. Wilson, T. Taniguchi, K. Watanabe, W. Yao, D. Xiao, M. A. McGuire, K.-M. C. Fu, and X. Xu, *Nano Lett.* **18**, 3823–3828 (2018).
- ⁵ D. Zhong, K. L. Seyler, X. Linpeng, R. Cheng, N. Sivadas, B. Huang, E. Schmidgall, T. Taniguchi, K. Watanabe, M. A. McGuire, W. Yao, D. Xiao, K.-M. C. Fu, and X. Xu, *Sci. Adv.* **3**, e1603113 (2017).
- ⁶ A. Srivastava, M. Sidler, A. V. Allain, D. S. Lembke, A. Kis, and A. Imamoglu, *Nat. Phys.* **11**, 141–147 (2015).
- ⁷ Q. Zhang, S. A. Yang, W. Mi, Y. Cheng, and U. Schwingenschlögl, *Adv. Mater.* **28**, 959–966 (2016).
- ⁸ M. Ezawa, *Phys. Rev. Lett.* **109**, 055502 (2012).
- ⁹ M. Tahir, A. Manchon, K. Sabeeh, and U. Schwingenschlögl, *Appl. Phys. Lett.* **102**, 162412 (2013).
- ¹⁰ C. J. Tabert and E. J. Nicol, *Phys. Rev. B* **87**, 235426 (2013).
- ¹¹ W. Yao, D. Xiao, and Q. Niu, *Phys. Rev. B* **77**, 235406 (2008).
- ¹² B. V. Duppen, P. Vasilopoulos, and F. M. Peeters, *Phys. Rev. B* **90**, 035142 (2014).
- ¹³ C. J. Tabert and E. J. Nicol, *Phys. Rev. B* **89**, 195410 (2014).
- ¹⁴ M. Mirzaei, T. Vazifeshenas, T. Salavati-fard, M. Farmanbar, and B. Tanatar, *Phys. Rev. B* **98**, 045429 (2018).
- ¹⁵ C. J. Tabert and E. J. Nicol, *Phys. Rev. Lett.* **110**, 197402 (2013).
- ¹⁶ Y. Ye, J. Xiao, H. Wang, Z. Ye, H. Zhu, M. Zhao, Y. Wang, J. Zhao, X. Yin, and X. Zhang, *Nat. Nanotech.* **11**, 598–602 (2016).
- ¹⁷ V. T. Renard, B. A. Piot, X. Waintal, G. Fleury, D. Cooper, Y. Niida, D. Tregurtha, F. Fujiwara, Y. Hirayama, and K. Takashina, *Nat. Commun.* **6**, 7230 (2015).
- ¹⁸ Y. P. Shkolnikov, K. Vakili, E. P. De Poortere, and M. Shayegan, *Phys. Rev. Lett.* **92**, 246804 (2004).
- ¹⁹ M. Settnes, J. H. Garcia, and S. Roche, *2D Mater.* **4**, 031006 (2017).
- ²⁰ J. M. Marmolejo-Tejada, J. H. García, M. D. Petrović, P.-H. Chang, X.-L. Sheng, A. Cresti, P. Plecháč, S. Roche, and B. K. Nikolić, *J. Phys.: Mater.* **1**, 015006 (2018).
- ²¹ H. Zeng, J. Dai, Y. Wand, D. Xiao, and X. Cui, *Nat. Nanotech.* **7**, 490–493 (2012).
- ²² J. Kim, X. Hong, C. Jin, S.-F. Shi, C.-Y. S. Chang, M.-Y. Chiu, L.-J. Li, and F. Wang, *Science* **346**, 1205–1208 (2014).
- ²³ E. J. Sie, J. W. McIver, Y.-H. Lee, L. Fu, J. Kong, and N. Gedik, *Nat. Mater.* **14**, 290–294 (2015).
- ²⁴ Y. Li, J. Ludwig, T. Low, A. Chernikov, X. Cui, G. Arefe, Y. D. Kim, A. M. van der Zander, A. Rigosi, H. M. Hill, S. H. Kim, J. Hone, Z. Li, D. Smirnov, and T. F. Heinz, *Phys. Rev. Lett.* **113**, 266804 (2014).
- ²⁵ G. Aivazian, Z. Gong, A. M. Jones, R.-L. Chu, J. Yan, D. G. Mandrus, C. Zhang, D. Cobden, W. Yao, and X. Xu, *Nat. Phys.* **11**, 148–152 (2015).
- ²⁶ A. Arora, R. Schmidt, R. Schneider, M. R. Molas, I. Breslavetz, M. Potemski, and R. Bratschitsch, *Nano Lett.* **16**, 3624–3629 (2016).
- ²⁷ X. Chen, L. Zhong, X. Li, and J. Qi, *Nanoscale* **9**, 2188–2194 (2017).
- ²⁸ C. Zhao, T. Norden, P. Zhang, P. Zhao, Y. Cheng, F. Sun, J. P. Parry, P. Taheri, J. Wang, Y. Yang, T. Scrace, K. Kang, S. Yang, G.-X. Miao, R. Sabirianov, G. Kioseoglou, W. Huang, A. Petrou, and H. Zeng, *Nat. Nanotech.* **12**, 757–763 (2017).
- ²⁹ G. Kresse and J. Furthmüller, *Comput. Mater. Sci.* **6**, 15–50 (1996).
- ³⁰ G. Kresse and J. Furthmüller, *Phys. Rev. B* **54**, 11169 (1996).
- ³¹ J. P. Perdew, K. Burke, and M. Ernzerhof, *Phys. Rev. Lett.* **77**, 3865 (1996).
- ³² P. E. Blöchl, *Phys. Rev. B* **50**, 17953 (1994).
- ³³ S. Grimme, J. Antony, S. Ehrlich, and S. Krieg, *J. Chem. Phys.* **132**, 154104 (2010).
- ³⁴ S. L. Dudarev, G. A. Botton, S. Y. Sarasov, C. J. Humphreys, and A. P. Sutton, *Phys. Rev. B* **57**, 1505–1509 (1998).

- ³⁵ J. L. Lado and J. Fernández-Rossier, *2D Mater.* **4**, 035002 (2017).
- ³⁶ B. Huang, G. Clark, E. Navarro-Moratalla, D. R. Klein, R. Cheng, K. L. Seyler, D. Zhong, E. Schmidgall, M. A. McGuire, D. H. Cobden, W. Yao, D. Xiao, P. Jarillo-Herrero, and X. Xu, *Nature* **8**, 270–273 (2017).
- ³⁷ T. Song, X. Cai, M. W.-Y. Tu, X. Zhang, B. Huang, N. P. Wilson, K. L. Seyler, L. Zhu, T. Taniguchi, K. Watanabe, M. A. McGuire, D. H. Cobden, D. Xiao, W. Yao and X. Xu, *Science* **360**, 1214–1218 (2018).
- ³⁸ L. Ji, J. Shi, Z.Y. Zhang, J. Wang, J. Zhang, C. Tao, and H. Cao, *J. Chem. Phys.* **148**, 014704 (2018).
- ³⁹ Q. Yue, J. Kang, Z. Shao, X. Zhang, S. Chang, G. Wang, S. Qin, and J. li, *Phys. Lett. A* **376**, 1166–1170 (2012).
- ⁴⁰ C. H. Chang, X. Fan, S. H. Lin, and J. L. Guo, *Phys. Rev. B* **88**, 195420 (2013).
- ⁴¹ M. Ghorbani-Asi, S. Borini, A. Kuc, and T. Heine, *Phys. Rev. B* **87**, 235434 (2013).
- ⁴² A. Hallal, F. Ibrahim, H. Yang, S. Roche, and M. Chshiev, *2D Mater.* **4**, 025074 (2017).
- ⁴³ A. Dyrdal and J. Barnaś, *2D Mater.* **4**, 034003 (2017).
- ⁴⁴ See Supplemental Material at [URL] for details of other influencing factors on the valley splitting of the $\text{WSe}_2/\text{CrI}_3$ and $\text{CrI}_3/\text{WSe}_2/\text{CrI}_3$.
- ⁴⁵ F. Guinea, M. I. Katsnelson, M. A. H. Vozmediano, *Phys. Rev. B* **77**, 075422 (2008).
- ⁴⁶ K. Kośmider, J. W. González, and J. Fernández-Rossier, *Phys. Rev. B* **88**, 245436 (2013).
- ⁴⁷ A. Kormányos, V. Zólyomi, N. D. Drummond, and G. Burkard, *Phys. Rev. X* **4**, 011034 (2014).
- ⁴⁸ Y. Zhao, J. Qiao, P. Yu, Z. Hu, Z. Lin, S. P. Lau, Z. Liu, W. Ji, and Y. Chai, *Adv. Mater.* **28**, 2399–2407 (2016).
- ⁴⁹ P. Ci, Y. Chen, J. Kang, R. Suzuki, H. S. Choe, J. Suh, C. Ko, T. Park, K. Shen, Y. Iwasa, S. Tongay, J. W. Ager III, L. W. Wang, and J. Wu, *Nano Lett.* **17**, 4982–4988 (2017).
- ⁵⁰ H. Kasai, K. Tolborg, M. Sist, J. Zhang, V. R. Hathwar, M. Ø. Filsø, K. Sugimoto, J. Overgaard, E. Nishibori, and B. B. Iversen, *Nat. Mater.* **17**, 249–252 (2018).
- ⁵¹ N. Sivadas, S. Okamoto, X. Xu, C. J. Fennie, and D. Xiao, *Nano Lett.* **18**, 7658–7664 (2018).